Durgun, E.; Ciraci, S.; Yildirim, T. (2008): Functionalization of carbon-based nanostructures with light transition-metal atoms for hydrogen storage. *Phys. Rev. B*, vol. 77, pp. 085405–1–085405–9.

Elias, D. C.; Nair, R. R.; Mohiuddin, T. M. G.; Morozov, S. V.; Blake, P.; Halsall, M. P.; Ferrari, A. C.; Boukhvalov, D. W.; Katsnelson, M. I.; Geim, A. K.; Novoselov, K. S. (2009): Control of graphene's properties by reversible hydrogenation: evidence for graphane. *Science*, vol. 323, pp. 610–613.

Feynman, R. P. (1939): Forces in molecules. *Phys. Rev.*, vol. 56, pp. 340–343.

Frisch, M. J.; Trucks, G. W.; Schlegel, H. B.; Scuseria, G. E.; Robb, M. A.; Cheeseman, J. R.; Montgomery Jr, J. A.; Vreven, T.; Kudin, K. N.; Burant, J. C.; Millam, J. M.; Iyengar, S. S.; Tomasi, J.; Barone, V.; Mennucci, B.; Cossi, M.; Scalmani, G.; Rega, N.; Petersson, G. A.; Nakatsuji, H.; Hada, M.; Ehara, M.; Toyota, K.; Fukuda, R.; Hasegawa, J.; Ishida, M.; Nakajima, T.; Honda, Y.; Kitao, O.; Nakai, H.; Klene, M.; Li, X.; Knox, J. E.; Hratchian, H. P.; Cross, J. B.; Adamo, C.; Jaramillo, J.; Gomperts, R.; Stratmann, R. E.; Yazyev, O.; Austin, A. J.; Cammi, R.; Pomelli, C.; Ochterski, J. W.; Ayala, P. Y.; Morokuma, K.; Voth, G. A.; Salvador, P.; Dannenberg, J. J.; Zakrzewski, V. G.; Dapprich, S.; Daniels, A. D.; Strain, M. C.; Farkas, O.; Malick, D. K.; Rabuck, A. D.; Raghavachari, K.; Foresman, J. B.; Ortiz, J. V.; Cui, Q.; Baboul, A. G.; Clifford, S.; Cioslowski, J.; Stefanov, B. B.; Liu, G.; Liashenko, A.; Piskorz, P.; Komaromi, I.; Martin, R. L.; Fox, D. J.; Keith, T.; Al-Laham, M. A.; Peng, C. Y.; Nanayakkara, A.; Challacombe, M.; Gill, P. M. W.; Johnson, B.; Chen, W.; Wong, M. W.; Gonzalez, C.; Pople, J. A. (2004): computer code GAUSSIAN 03 Rev. D.01, 2004.

Guisineger, N. P.; Rutter, G. M.; Crain, J. N.; First, P. N.; Stroscio, J. A. (2009): Exposure of epitaxial graphene on SiC(0001) to atomic hydrogen. *Nano Lett.*, vol. 9, pp. 1462–1466.

Gupta, B. K.; Srivastava, O. N. (2000): Synthesis and hydrogenation behaviour of graphitic nanofibres. *Int. J. Hydrogen Energy*, vol. 25, pp. 825–830.

Gupta, B. K.; Srivastava, O. N. (2001): Further studies on microstructural characterization and hydrogenation behaviour of graphitic nanofibres. *Int. J. Hydrogen Energy*, vol. 26, pp. 857–862.

Hanasaki, I.; Nakamura, A.; Yonebayashi, T.; Kawano, S. (2008): Structure and stability of water chain in a carbon nanotube. *J. Phys. Condens. Matter.*, vol. 20, pp. 015213–1–015213–7.

Herzberg, G. (1969): Dissociation energy and ionization potential of molecular hydrogen. *Phys. Rev. Lett.*, vol. 23, pp. 1081–1083.

Hirscher, M.; Becher, M.; Haluska, M.; Dettlaff-Weglikowska, U.; Quintel, A.; Duesberg, G. S.; Choi, Y.-M.; Downes, P.; Hulman, M.; Roth, S.; Stepanek, I.; Bernier, P. (2001): Hydrogen storage in sonicated carbon materials. *Appl. Phys. A*, vol. 72, pp. 129–132.

Jeloacia, L.; Sidis, V. (1999):   DFT investigation of the adsorption of atomic hydrogen on a cluster-model graphite surface. *Chem. Phys. Lett.*, vol. 300, pp. 157–162.

Kawano, S. (1998): Molecular dynamics of rupture phenomena in a liquid thread. *Phys. Rev. E*, vol. 58, pp. 4468–4472.

Leforestier, C. (1978):   Classical trajectories using the full *ab initio* potential energy surface $H^- + CH_4 \rightarrow CH_4 + H^-$. *J. Chem. Phys.*, vol. 68, pp. 4406–4410.

Li, J.; Furuta, T.; Goto, H.; Ohashi, T.; Fujiwara, Y.; Yip, S. (2003):   Theoretical evaluation of hydrogen storage capacity in pure carbon nanostructures. *J. Chem. Phys.*, vol. 119, pp. 2376–2385.

Liu, C.; Fan, Y. Y.; Liu, M.; Cong, T. H.; Cheng, H. M.; Dresselhaus, M. S. (1999): Hydrogen storage in single-walled carbon nanotubes at room temperature. *Science*, vol. 286, pp. 1127–1129.

Miura, Y.; Kasai, H.; Diño, W. A.; Nakanishi, H.; Sugimoto, T. (2003):   First principles studies on the interaction of a hydrogen atom with a single-walled carbon nanotube. *Jpn. J. Appl. Phys.*, vol. 42, pp. 4626–4629.

Nakano, H.; Ohta, H.; Yokoe, A.; Doi, K.; Tachibana, A. (2006): First-principle molecular-dynamics study of hydrogen adsorption on an aluminum-doped carbon nanotube. *J. Power Sources*, vol. 163, pp. 125–134.

Nishimiya, N.; Ishigaki, K.; Takikawa, H.; Ikeda, M.; Hibi, Y.; Sakakibara, T.; Matsumoto, A.; Tsutsumi, K. (2002):   Hydrogen sorption by single-walled carbon nanotubes prepared by a torch arc method. *J. Alloys Compd.*, vol. 339, pp. 275–282.

Okamoto, Y.; Miyamoto, Y. (2001):   *Ab initio* investigation of physisorption of molecular hydrogen on planar and curved graphenes. *J. Phys. Chem. B*, vol. 105, pp. 3470–3474.

Patchkovskii, S.; Tse, J. S.; Yurchenko, S. N.; Zhechkov, L.; Heine, T.; Seifert, G. (2005):   Graphene nanostructures as tunable storage media for molecular hydrogen. *Proc. Nat. Acad. Sci. U.S.A.*, vol. 102, pp. 10439–10444.

Rappé, A. K.; Casewit, C. J.; Colwell, K. S.; Goddard III, W. A.; Skiff, W. M. (1992):   UFF, a full periodic table force field for molecular mechanics and molecular dynamics simulations. *J. Am. Chem. Soc.*, vol. 114, pp. 10024–10035.

Riedl, C.; Coletti, C.; Iwasaki, T.; Zakharov, A. A.; Starke, U. (2009): Quasi-free-standing epitaxial graphene on SiC obtained by hydrogen intercalation. *Phys. Rev. Lett.*, vol. 103, pp. 246804–1–246804–4.

Riedl, C.; Coletti, C.; Starke, U. (2010): Structural and electronic properties of epitaxial graphene on SiC(0001): a review of growth, characterization, transfer doping and hydrogen intercalation. *J. Phys. D: Appl. Phys.*, vol. 43, pp. 374009–1–374009–15.

Schmitt, U. W.; Voth, G. A. (1998): Multistate empirical valence bond model for proton transport in water. *J. Phys. Chem. B*, vol. 102, pp. 5547–5551.

Sha, X.; Jackson, B. (2001): First-principles study of the structural and energetic properties of H atoms on a graphite (0001) surface. *Surf. Sci.*, vol. 496, pp. 318–330.

Ströbel, R.; Jörissen, L.; Schliermann, T.; Trapp, V.; Schütz, W.; Bohmhammel, K.; Wolf, G.; Garche, J. (1999): Hydrogen adsorption on carbon materials. *J. Power Sources*, vol. 84, pp. 221–224.

Szabo, A.; Ostlund, N. S. (1982): *Modern Quantum Chemistry*. Macmillan Publishing, New York.

Tada, K.; Furuya, S.; Watanabe, K. (2001): *Ab initio* study of hydrogen adsorption to single-walled carbon nanotubes. *Phys. Rev. B*, vol. 63, pp. 155405–1–155405–4.

Virojanadara, C.; Yakimova, R.; Zakharov, A. A.; Johansson, L. I. (2010): Large homogeneous mono-/bi-layer graphene on 6H-SiC(0001) and buffer layer elimination. *J. Phys. D: Appl. Phys.*, vol. 43, pp. 374010–1–374010–13.

Virojanadara, C.; Zakharov, A. A.; Yakimova, R.; Johansson, L. I. (2010): Buffer layer free large area bi-layer graphene on SiC(0001). *Surf. Sci. Lett.*, vol. 604, pp. L4–L7.

Warshel, A.; Weiss, R. M. (1980): An empirical valence bond approach for comparing reactions in solutions and in enzymes. *J. Am. Chem. Soc.*, vol. 102, pp. 6218–6226.

Witmer, E. E. (1926): Critical potentials and the heat of dissociation of hydrogen as determined from its ultra-violet band spectrum. *Proc. Nat. Acad. Sci. U.S.A.*, vol. 12, pp. 238–244.

Xu, W.-C.; Takahashi, K.; Matsuo, Y.; Hattori, Y.; Kumagai, M.; Ishiyama, S.; Kaneko, K.; Iijima, S. (2007): Investigation of hydrogen storage capacity of various carbon materials. *Int. J. Hydrogen Energy*, vol. 32, pp. 2504–2512.

Yang, R. T. (2000): Hydrogen storage by alkali-doped carbon nanotubes-revisited. *Carbon*, vol. 38, pp. 623–641.

Characterization of polymer structures based on Burnside's lemma

Kentaro Doi, Keigo Kato, and Satoyuki Kawano[*]

Department of Mechanical Science and Bioengineering, Graduate School of Engineering Science,
Osaka University, Osaka 560-8531, Japan
(Received 23 August 2010; published 19 July 2011)

Polymer structure modeling is a trend of recent material sciences. Developments of computational science and nanotechnology make it possible to predict properties of complicated molecular structures. Many theoretical and computational methods have succeeded in elucidating the nature of polymer structures. It is not always best to model whole complicated structures depending on computer capabilities. Significant properties of materials may be manifested in simple structural aspects. In the present study, characteristics of a polymer structure are investigated by applying Burnside's lemma to the modeling procedure. This method is expected to be available to model polymers or molecular crystals in which functional groups play an important role in expressing their functions. Every structure under the symmetry and periodicity is counted completely and the energy distribution caused by the conformations of functional groups can be clarified. The detailed procedure is introduced and the present method is applied to a problem for investigating molecular structures of sulfonated poly(ether ether ketone) (SPEEK). SPEEK is focused on a candidate for proton exchange membranes in polymer electrolyte fuel cells. Sulfonic groups have a significant role in proton exchange membranes to make proton conduction channels. From our analysis, it is found that sulfonic groups tend to be dispersed in SPEEK membranes at their stable conditions. These are unfavorable characteristics for proton exchange membranes due to their difficulty to form desirable water channels inevitable for the high proton conductivity. This is one reason why SPEEK membranes are inferior to Nafion® membranes that express the highest performance as proton exchange membranes. Using the present method, experimental and theoretical results previously reported are confirmed and detailed characteristics are discussed in terms of structural simplicities.

I. INTRODUCTION

Recently, electron-conducting polymers and ion-conducting polymers have been attracting much attention [1–10]. They express various functions due to their specific structures or orientations of functional groups. In the case of electron-conducting polymers, overlaps of π orbitals above aromatic molecular surfaces enhance electronic conduction. Conformations of aromatic molecules strongly influence electronic conductivities. It is very important to control the molecular orientations in the fabrication processes. In ion-conducting polymers, carrier ions pass through water channels aggregated around functional groups. Especially in the case of proton conduction, protons appear to conduct through the water channels, changing the role of charge carrier with other H atoms of H_2O such as $H_3O^+ + H_2O \rightarrow H_2O + H_3O^+$. This mechanism is well known as the Grotthuss mechanism [11–18]. In this process, distributions of water molecules that concentrate around functional groups in polymers affect the proton conduction properties. Therefore, conformations of functional groups cause the formation of water channels that enhance high proton conduction. It is clear that molecular conformations significantly contribute to carrier conductivities in electron-conducting or ion-conducting polymers. However, there is a difficulty to modeling these polymers due to their complicated structures. In addition, it may be difficult to understand the origin of functions expressed by polymers even if their structures are modeled precisely.

On the other hand, some characteristics of polymers can be understood by simplified models. It is important to construct effective models from various perspectives to elucidate the mechanism. For instance, in the hopping conduction mechanism, it is suggested that electric carriers conduct through electronically or ionically polarized spaces. Therefore, it is meaningful to focus on an essence of carrier hopping process in polymer structures. Several methods to model polymer structures have been developed focusing on the behavior of functional groups [19–21]. Klein *et al.* [22–24] successfully counted and investigated molecular structures of alkane polymers. In their methods, Pólya's counting procedures were applied to investigate the polymer structures. In the present study, an original method is developed to model polymer structures focusing on functional groups that critically contribute to proton conduction. Our method assumes symmetries and periodicity to the polymer structures, although direct modeling of complicated molecular structures is a usual method. Using an imaginary polymer model, fundamental characteristics expressed by functional groups are discussed. In a closed symmetric system, all structures can be counted and the qualitative characteristics are elucidated from the energy distribution. This problem is treated as the similar way of color paintings on tiles.

In such procedures, energetically equivalent structures can be eliminated from all permutations based on the group theory. As a result, the computational efficiency is drastically improved compared with sequential counting of all possible permutations. The present method is applied to sulfonated poly(ether ether ketone) (SPEEK). In SPEEK membranes, sulfonic groups have a significant role in making proton

*kawano@me.es.osaka-u.ac.jp; http://bnf.me.es.osaka-u.ac.jp

011805-1

conduction channels [25–34]. Water molecules aggregate around sulfonic groups that are hydrophilic and enhance proton conduction. However, further proton conductivity and mechanical strength are required for the proton exchange membranes to endure the hard use under extraordinary conditions, such as fuel cells in electric vehicles. It is important to clarify the possibility of the materials. In the present model, one- and two-dimensional symmetric geometries in polymer bundles are treated. Energy distributions about molecular conformations are computed and the relationship between the structural stability and functional group conformations are clarified. In particular, it is found that sulfonic groups in SPEEK tend to be dispersed at their stable conditions and that concentrations of sulfonic groups that contribute to make water channels cannot be expected. On the other hand, bundles of the polymer chains tend to be energetically stable. The results derived from our mathematical approach reasonably agree with other computational results [35–38].

II. THEORETICAL DEVELOPMENT AND COMPUTATIONAL METHOD

In symmetric closed systems, structure modeling can be replaced by a tile painting problem. For example, Fig. 1 shows colored tiles that are sequentially aligned on a periodic band. These tiles are painted by four colors, such as red (R), green (G), blue (B), and yellow (Y). Considering the periodicity, symmetry equivalent colorings should be eliminated to count the number of nonequivalent colorings exactly. In order to treat this problem, there is an effective calculus based on the group theory and Burnside's lemma [39–43]. As shown in Fig. 1, the characteristics of a band are conserved under the symmetric operations, such as rotation, reflection, inversion, and their coupled operations, although color patterns seem to be changed by the operations. When each tile is painted by one of four colors, the number of nonequivalent patterns will be much less than that of all the combinations in which any symmetries and any boundary conditions are not considered. According to Burnside's lemma, the number of nonequivalent colorings under any symmetry can be counted mechanically.
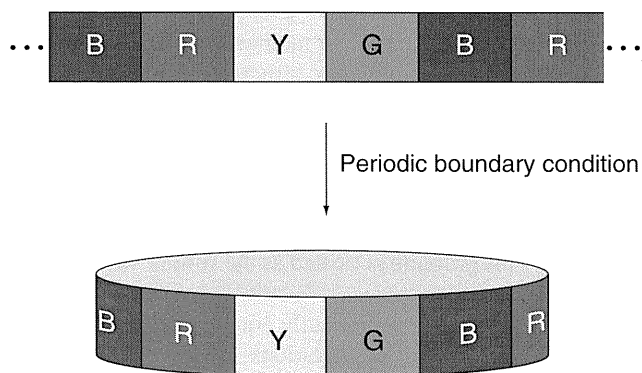

FIG. 1. (Color online) Illustration of color paintings by four colors, red (R), green (G), blue (B), and yellow (Y), on a one-dimensional segment, which is transformed to a band manifesting the periodicity.
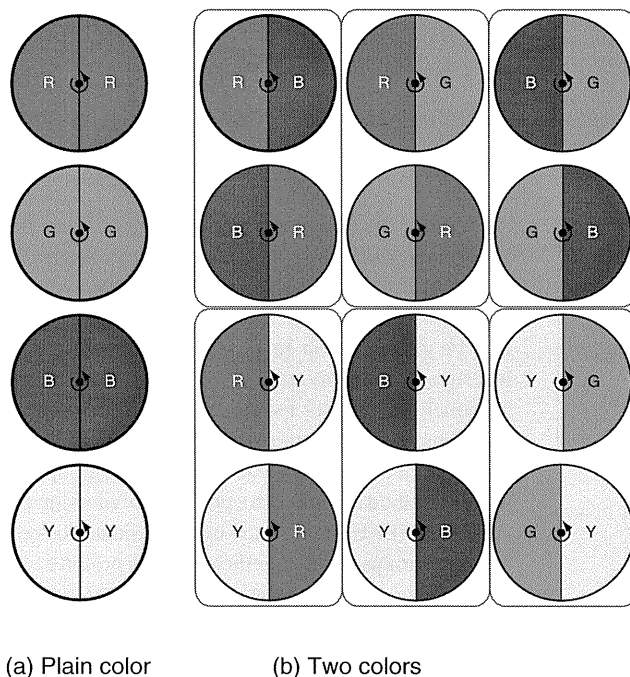

(a) Plain color   (b) Two colors

FIG. 2. (Color online) Painting on C_2 symmetric structure by (a) plain color and (b) two colors.

Burnside's lemma proves that the number of nonequivalent colorings N in a set C equals the average of the number of colorings fixed by the permutations in a group G [42]:

$$N(G) = \frac{1}{|G|} \sum_{f \in G} |C(f)|, \tag{1}$$

where C is a set of colorings such that $f * \mathbf{c} \in C$ for all symmetric operations $f \in G$ and all $\mathbf{c} \in C$. For example, characteristics are invariant under rotations in the cyclic group C_n when there are n tiles. In a C_2 symmetric structure as shown in Fig. 2, the principal rotational axis is perpendicular to the surface. There are 10 nonequivalent colorings to paint two parts of the surface due to four patterns by four plain colors and due to six patterns by two colors calculated from the combination of $_4C_2$. On the other hand, in accordance with Burnside's lemma, the number is counted simply as follows:

$$N(C_2) = \frac{1}{\text{the number of symmetric operations}}$$
$$\times [(\text{colorings conserved by identical operation } E)$$
$$+ (\text{colorings conserved by } C_2 \text{ rotation})]$$
$$= \frac{1}{2}(4^2 + 4) = 10. \tag{2}$$

That is, equivalent colorings which have six overlaps in this case are systematically eliminated from all the permutation: $4^2 = 16$. Furthermore, in a C_6 symmetric structure, nonequivalent colorings by four colors can be counted exactly:

$$N(C_6) = \frac{1}{6}[C(E) + C(C_6) + C(C_6^2)$$
$$+ C(C_6^3) + C(C_6^4) + C(C_6^5)]$$
$$= \frac{1}{6}(4^6 + 4 + 4^2 + 4^3 + 4^2 + 4) = 700. \tag{3}$$

TABLE I. Counts of four color paintings on a symmetric band: all permutation of 4^n, nonequivalent N colorings according to C_n symmetry based on Burnside's lemma, and their ratio. (n: number of tiles; N: number of colorings.)

				n		
	2	4	6	8	10	12
4^n	16	256	4960	65 536	1 048 596	16 777 216
$N(C_n)$	10	70	700	8230	104 968	1 398 500
$N(C_n)/4^n$	0.63	0.27	0.14	0.13	0.10	0.08

This number of nonequivalent colorings is much less than that of all the permutations 4^6 ($= 4960$) such that their ratio is 0.14 ($\simeq 700/4960$). Table I shows some comparisons between the nonequivalent colorings and all permutations for C_n symmetry. It is found that the ratio of nonequivalent colorings to all permutations is drastically reduced, e.g., the reduction ratio $N(C_n)/4^n \simeq 0.1$ for $n > 10$. This result indicates that the elimination of equivalent permutations is very effective in reducing the computational labor.

In this study, one- and two-dimensional molecular sequences are featured. Figure 3 shows monomer structures which are elements of SPEEK. It is assumed that the monomer structure is planar and that there are four conformations of sulfonic groups in the polymer chain. In other words, a sulfonic group is placed in one of four parts of the unit cell. The problem of counting the monomer sequences can be replaced by a four color painting problem. In order to simplify the complicated polymer structures, symmetries and periodicities are adjusted, focusing on the relative location of sulfonic groups. A monomer is packed in a unit cell; the cell parameters are set to $a_1 = 8.682$ Å, $a_2 = 5.643$ Å, and $a_3 = 17.040$ Å along the x, y, and z axis, respectively. These parameters are determined to eliminate the intermolecular repulsions and to minimize the total energy. The polymer structure is constructed from combinations of these conformations. The present system has D_{nh} symmetry, which shows n-fold rotations about the principal axis, twofold rotations about the perpendicular axes, reflections in planes containing the principal axis, the reflection in the plane normal to the principal
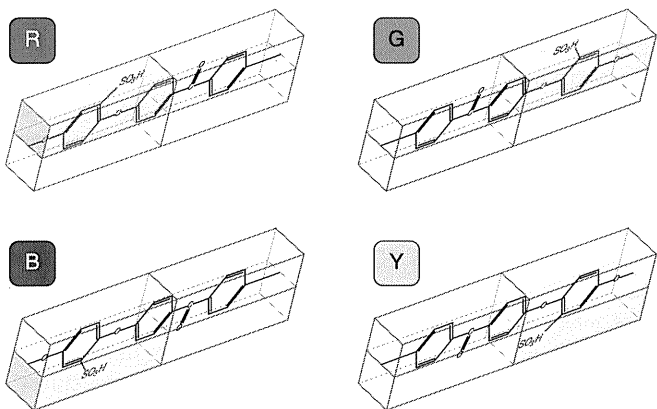

FIG. 3. (Color online) Illustrations of four conformations of the sulfonic group in SPEEK; the monomer is assumed to be a planar molecule on the xz plane and the main chain is along the z axis.

axis represented by the subscript h, and the inversion. In this case, the counting process seems to be complicated due to an increase in the number of symmetry operations, but the basic procedure is the same as that mentioned above based on Burnside's lemma, e.g., Eqs. (1)–(3). In the next section, results from counting up every nonequivalent n-mer chain are presented. Two-dimensional matrices in SPEEK bundles are discussed focusing on the relationship between conformations of sulfonic groups and their energy stabilities. The total energy of a system is evaluated using potential energy functions as follows [44–50]:

$$U_{\text{total}} = U_{\text{intra}} + U_{\text{inter}}, \tag{4}$$

$$U_{\text{intra}} = \sum^{N_r} K_r(r - r_{\text{eq}})^2 + \sum^{N_\theta} K_\theta(\theta - \theta_{\text{eq}})^2 + \sum^{N_d} \frac{V_n}{2}[1 + \cos(n\phi - \gamma)], \tag{5}$$

$$U_{\text{inter}} = \sum_{i<j}^{N_a} \left(\frac{A_{ij}}{R_{ij}^{12}} - \frac{B_{ij}}{R_{ij}^6} \right) + \sum_{i<j}^{N_a} \frac{q_i q_j}{4\pi \varepsilon_0 R_{ij}}, \tag{6}$$

where U_{intra} and U_{inter} denote intramolecular and intermolecular interactions, respectively. In the U_{intra}, bond energies are calculated for N_r bonds in which K_r is the force constant and $r - r_{\text{eq}}$ is the difference from the equivalent bond length; energies depending on bond angles are calculated for N_θ angles in which K_θ is the force constant and $\theta - \theta_{\text{eq}}$ is the difference from the equivalent angle; energies depending on dihedral angles are evaluated for N_d dihedral angles in which V_n is a force constant and $n\phi - \gamma$ is the difference from the equivalent angle. In the U_{inter}, the first and second terms respectively denote van der Waals (VDW) interactions and Coulomb interactions for N_a atoms, where R_{ij} is the distance between nuclei, A_{ij} and B_{ij} the constants depending on ion pairs, q_i the valence charge, and ε_0 the vacuum permittivity. A monomer structure of sulfonated ether ether ketone is optimized by summing the potential functions of Eqs. (5) and (6). In particular, intermolecular interactions between the polymer chains are evaluated by VDW and Coulomb interactions according to Eq. (6) and their computations are carried out for a minimal size of the supercell. As a schematic of the supercell is shown in Fig. 4(a), conformations of sulfonated ether ether ketone in the supercell are represented. The convergence of the intermolecular interactions is evaluated by

$$\delta_n = \frac{E_{\text{inter}}(n + 1) - E_{\text{inter}}(n)}{E_{\text{inter}}(n) - E_{\text{inter}}(n - 1)} - 1, \tag{7}$$

where $E_{\text{inter}}(n)$ denotes the energy of a system that consists of n unit cells. The energy convergence is determined by $|\delta_n| < \epsilon$ for integer m such that $n > m$. The energy evaluation is performed for finite systems without considering periodicities to directly estimate the effective range of intermolecular interactions. These evaluations are summarized in Table II. In this study, the small value ϵ is set to 0.05 and then the supercell is determined as the integral multiple of the unit cells: $(n_x, n_y, n_z) = (3, 3, 1)$ as shown in Fig. 4. Intermolecular interactions along the polymer main chain (z axis) are so weak that conformations of sulfonic groups are not effective for intermolecular interactions along the z axis. Therefore,
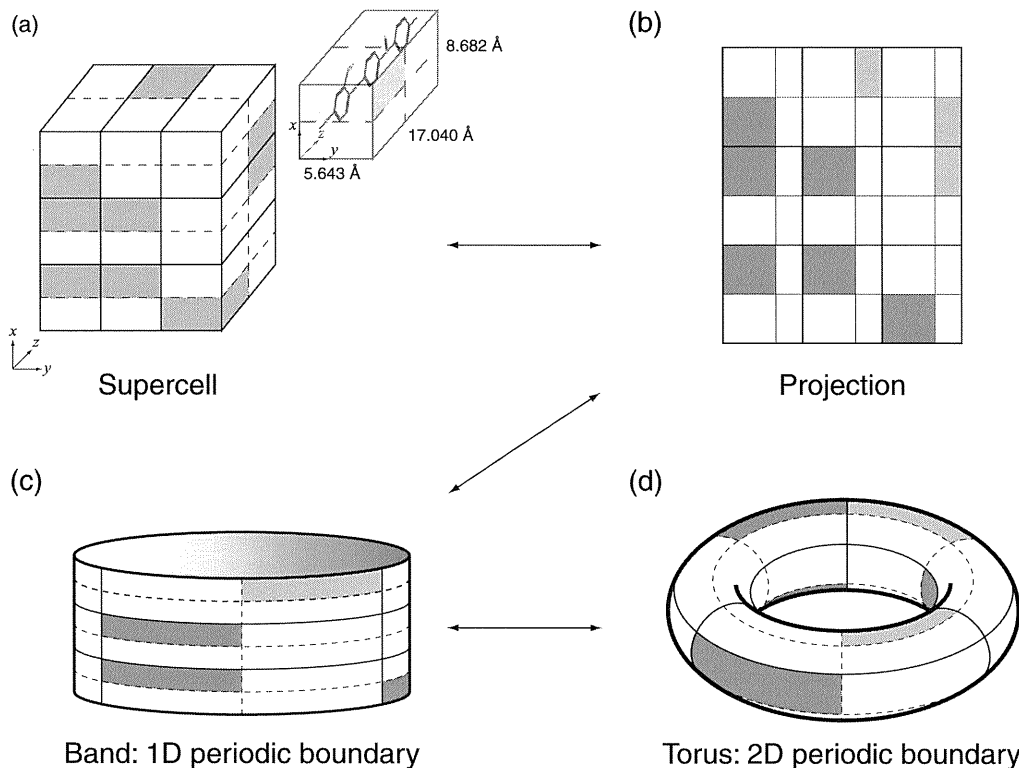
FIG. 4. Schematic illustrations of continuous transformations between (a) supercell, (b) projection on a plane, (c) band, and (d) torus.

conformations of the sulfonic groups in the vertical plane (xy plane) dominate energy stabilities. The intermolecular energy evaluations are performed with a three-dimensional periodic boundary condition. Figure 4 shows a concept of topological transformation of the supercell. Figure 4(b) is a projection of the supercell [Fig. 4(a)] onto the xy plane. Here, structural characteristics are attributed to the sulfonic group conformations in a two-dimensional plane, such as a cross section of the polymer chain bundle. Focusing on four conformations of a sulfonic group, $D_{3h} \times D_{3h}$ symmetry is applied to count up all the nonequivalent structures. As shown in Figs. 4(b)–4(d), the two-dimensional periodic structure is represented by the torus symmetry that is continuously transformed from the two-dimensional plane.

TABLE II. Intermolecular interaction energy, the difference, and convergence.

	$E_{inter}(n)$ (kJ/mol)	$E_{inter}(n) - E_{inter}(n-1)$ (kJ/mol)	δ_n
n_x			
2	−387	−387	0.118
3	−820	−433	0.002
4	−1254	−433	
n_y			
2	−387	−387	0.152
3	−833	−446	0.015
4	−1285	−452	
n_z			
2	−387	−387	0.005
3	−774	−389	

III. RESULTS AND DISCUSSION

Table III shows the number of nonequivalent four-color paintings counted according to D_{nh} symmetry. First, calculations for one-dimensional periodic sequences shown in Fig. 1 were carried out. For comparison, the ratio of $N(D_{nh})/4^n$ is also presented in Table III. It is found that the number of nonequivalent sequences increases exponentially and the increase is approximately presented as a function of n: $2^{1.7n-2.3}$. This counting method based on Burnside's lemma is more efficient than counting all the permutations. The ratio becomes the order of 10^{-2} for $n > 3$. Computational labor can be drastically reduced using the effective counting procedure in the symmetric structures.

Next, conformations of functional groups in two-dimensional matrices are investigated. Sulfonic groups in the supercell composed of $3 \times 3 \times 1$ unit cells are treated and their distributions are counted completely according to D_{3h} symmetry. As mentioned above, this thing can be replaced by a problem to count the number of ways of tile colorings on the 3×3 periodic matrix. This two-dimensional periodic matrix of $D_{3h} \times D_{3h}$ symmetry is topologically transformed to a torus symmetry as shown in Fig. 4. Figure 5 shows the principal axes of $C1$ and $C2$ in the torus symmetry. Rotations along $C1$ and $C2$ correspond to periodic translations along the y and x axis of the supercell, respectively. The group order is provided by tensor products of each vector space. In the same way as the one-dimensional case, nonequivalent structures can be counted completely. The number of nonequivalent structures is concluded to be 7296, which is much less than 4^9 ($= 262\,144$). Intermolecular energy computations for the nonequivalent structures were performed. Figure 6

TABLE III. Nonequivalent counts according to D_{3h} symmetry and proportion to permutation of 4^n.

	n														
	1	2	3	4	5	6	7	8	9	10	11	12	13	14	15
$N(D_{nh})$	1	4	6	23	52	194	586	2131	7285	26 524	95 326	350 738	1 290 556	4 798 174	17 895 703
$N(D_{nh})/4^n$	0.25	0.25	0.09	0.09	0.05	0.05	0.04	0.03	0.03	0.03	0.02	0.02	0.02	0.02	0.02

shows the relationship between the polymer structures and the intermolecular energies. For comparison, the total energies of the nonequivalent molecular structures were computed using molecular mechanics (MM) method [48]. The abscissa shows the sequential number that is sorted by the energies resulting from MM computations. The results from the present computations are corrected by the energy shift. The computational accuracy of MM methods is higher than that of the present method, although more computational time is consumed, because all intermolecular and intramolecular interactions are counted and the long-range intermolecular interactions are considered up to the cutoff distances: 10 Å for VDW interactions and 30 Å for Coulomb interactions [44–50]. Therefore, the difference between the MM and our results was corrected by the energy shift. The mean energies were estimated from each energy distribution, such as $\overline{E}$ resulting from the present study and $\overline{E}_{MM}$ from MM computations. The difference between the two was calculated as

$$\overline{E} - \overline{E}_{MM} = \frac{1}{N}\sum_{i=1}^{N} E_i - \frac{1}{N}\sum_{i=1}^{N} E_{MM,i}$$

$$= \frac{1}{N}\sum_{i=1}^{N}(E_i - E_{MM,i}) \equiv \overline{\Delta E}, \qquad (8)$$

where $N = 7296$ and $\overline{\Delta E}$ was estimated as 1268 kJ/mol. As a result of the parallel shift, the present result was in good agreement with the result of MM computations. The distribution is clearly represented by our simple procedure. The difference between the two is caused by the long-range intermolecular interactions ignored out of the nearest neighbors in the present method. However, this ignorance is not so serious to maintain the qualitative characteristics. The present computations, which include intermolecular interactions only between the nearest neighbors, can represent the characteristics resulting from more laborious methods.

Figure 7 shows the energy distributions depending on sulfonic group conformations. For comparison, results from MM computations are presented in the same figure. The difference between each distribution was corrected by the procedure mentioned above. Shapes of these energy distributions showing peaks between −9000 and −6000 kJ/mol agreed with each other. It is clear that nonequivalent stable or unstable structures are relatively fewer than energetically intermediate structures. The whole picture of structural stability can be clarified using the present method. Structural characteristics are statistically elucidated, although discussions are constrained by the symmetry. Figure 8 shows schematic illustrations of sulfonic group conformations. As shown in Fig. 8(a), each block indicates positions of sulfonic groups along the z axis: front upper, front lower, rear upper, and rear lower sides. A part including a sulfonic group is painted in a gray color. As shown in Fig. 8(b), polymer structures become unstable as their conformations are highly oriented. This tendency is
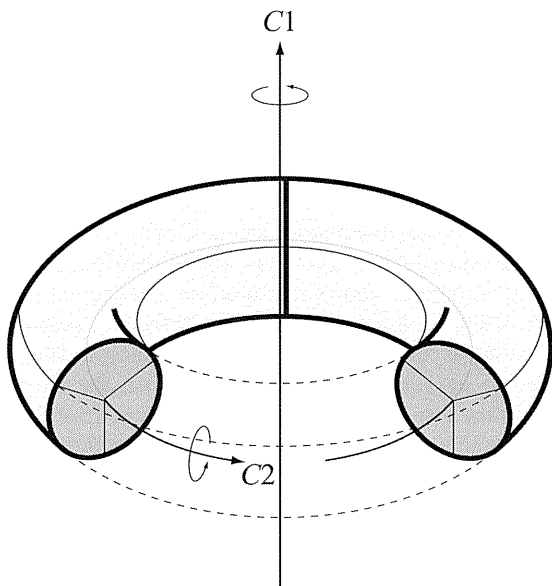

FIG. 5. Torus of two-dimensional D_{3h} symmetry, which represents the 3×3 matrix; $C1$ and $C2$ are principal axes of each vector space.
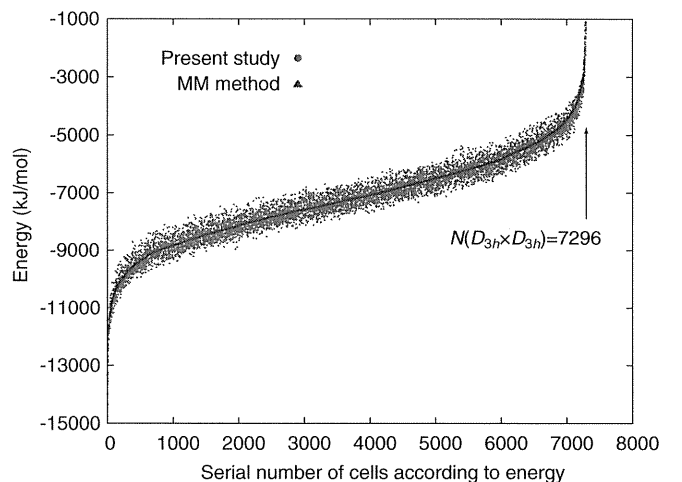

FIG. 6. (Color online) Comparison of energies between the present method (closed purple circle) and MM method (closed blue triangle); plots of the present result are shifted by 1268 kJ/mol each.
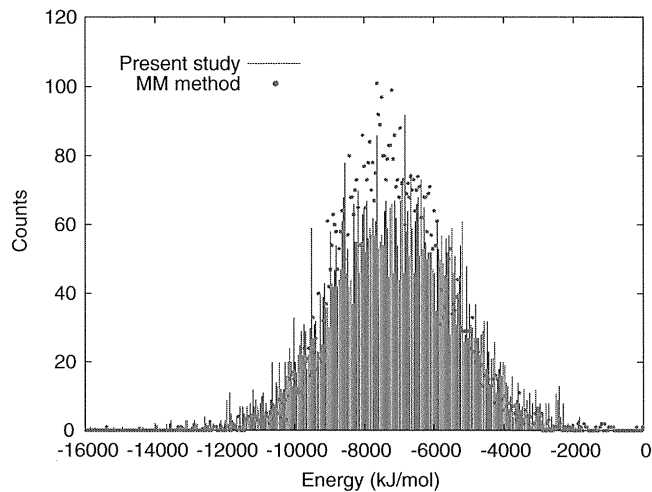
FIG. 7. (Color online) Energy distribution of $3 \times 3 \times 1$ nonequivalent periodic structures of the SPEEK model; the present results are shifted by 1268 kJ/mol each.

remarkable at the highest 10% of the energy distribution. However, the polymer chains tend to be attractive by their intermolecular interactions. Therefore, SPEEK is stable with forming the polymer chain bundles. At intermediate energy regions as shown in Figs. 8(c) and 8(d), partial concentrations or sparse regions of sulfonic groups are observed in various polymorphisms. This variety contributes to the high population in the distribution and they are nonequivalent to each other. On the other hand, as shown in Figs. 8(e) and 8(f), in the lowest 10% of the energy distribution, sulfonic groups are stabilized in polymer bundle structures and, in this case, they tend to be located to avoid concentrations. It is clarified that, in the case of SPEEK, sulfonic groups usually avoid their concentrations, although bundles of the polymer chains make their structures energetically stable.

Figure 9 shows the radial distribution functions of sulfonic groups in SPEEK. The function is evaluated by

$$g(r) = \frac{\overline{N(r)}}{4\pi r^2 \rho \Delta r}, \tag{9}$$

where $\overline{N(r)}$ is the number of sulfonic groups in a spherical shell between r and $r + \Delta r$, which is averaged over each energy region; ρ is the density of sulfonic groups in SPEEK. Distances between sulfur atoms in sulfonic groups were measured. The thickness of the spherical shell Δr was set to 0.85 Å. The value of ρ was set to 8.47×10^{-2} g/cm^3, as determined from the optimized unit cell. As shown in Fig. 9, the radial distribution functions were calculated for several regions in the energy distribution. The low-, high-, and intermediate-energy regions correspond to those shown in Fig. 7. In the high-energy structures, sulfonic groups concentrate at a distance of 5.5 Å. In addition, the second and third nearest peaks are at 7.2 and 8.9 Å, respectively. Amounts of the second and third nearest-neighbor sulfonic groups are fewer than those of the nearest one. However, peaks at a long distance seem to be affected by the periodicity. In particular, peaks out to $r = 8.46$ Å may contain the effect of the periodicity due to the half-length of the shortest side 16.92 Å along the y axis on the
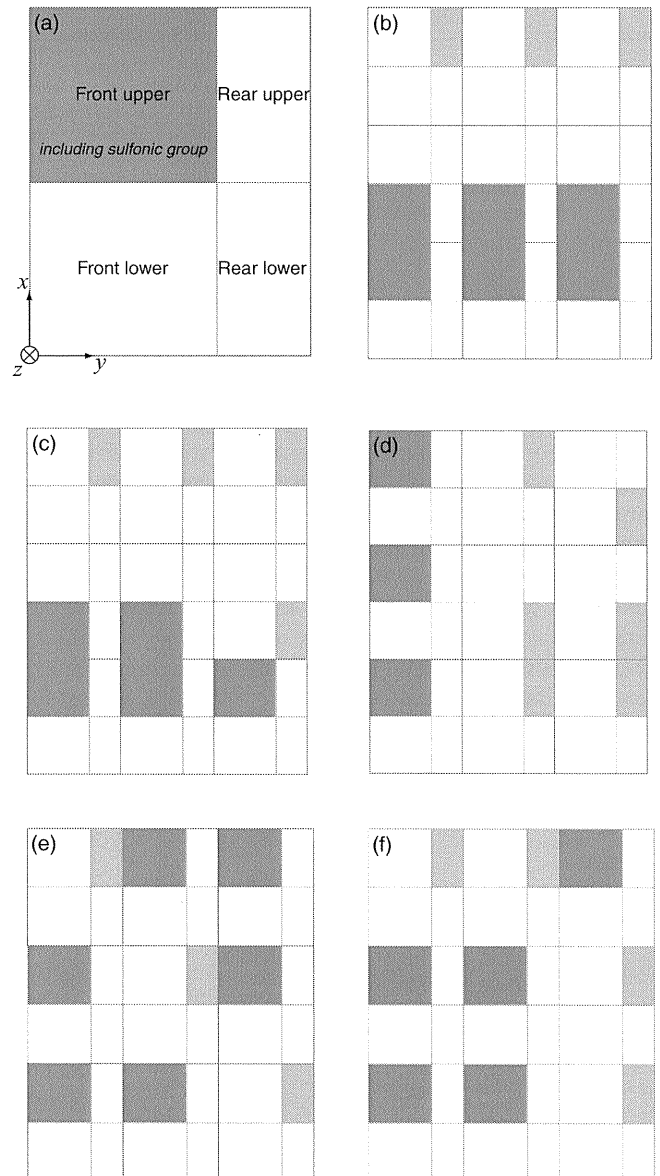

FIG. 8. (a) Schematic of sulfonic group conformation in SPEEK, (b) the high-energy placements, (c), (d) energetically intermediate conformations, and (e), (f) the low-energy conformations.

supercell. Therefore, discussions are especially focused on the first and second peaks of $g(r)$. The radial distribution of the low-energy structures shows that the first and second nearest peaks are observed at 5.5 and 7.2 Å, respectively. These points are the same as those of high-energy structures. However, quantities of $g(r)$ are different depending on the structural stability. In the low-energy structures, a peak of 15.9 at 5.5 Å is lower than that of 22.9 in the high-energy structures. On the other hand, the second peak of 13.8 at 7.2 Å is higher than that of 11.6 in the high-energy structures. The distribution of the intermediate-energy region, which is focused on 10% around the peak of distribution, is similar to that of the low-energy region, although the values at the first and second peaks are a little larger than those in the case of low-energy structures. From Fig. 9, the relationship between the energy stabilities and the distributions of sulfonic groups is elucidated. These results
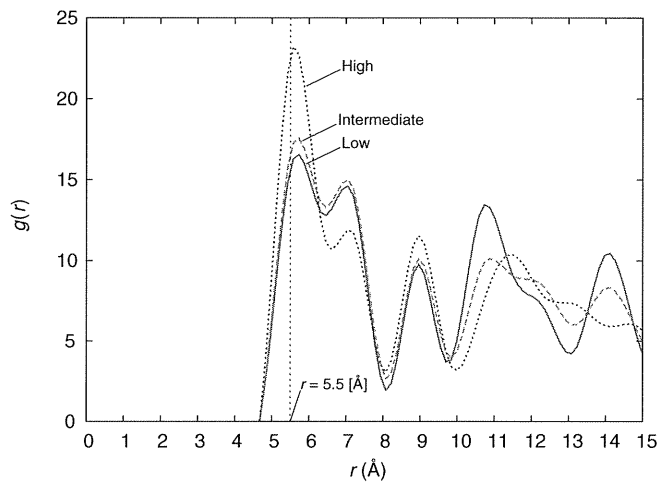
FIG. 9. (Color online) Radial distribution functions of sulfonic groups in $3 \times 3 \times 1$ periodic structures of SPEEK: analyses for 10% of the lowest (solid red line), intermediate (dashed green line), and highest energy structures (dotted blue line). These plots are interpolated by cubic spline. The peak point at $r = 5.5$ Å reasonably agrees with other results in Refs. [35] and [37].

indicate that the systems become stable as sulfonic groups are located sparsely. In addition, highly oriented placements and high concentrations of sulfonic groups in SPEEK make the polymer structures relatively unstable. These distribution characteristics of sulfonic groups correspond to the schematic visualizations in Fig. 8. Furthermore, the radial distribution functions are in agreement with results from other researchers using the coarse-grained [35] and atomistic [37] molecular dynamics methods. In the real polymer structures, it is implied that main chains are concentrated locally with cross-linking and that sulfonic groups are distributed stably in these domains. In addition, in other computational methods depending on a concept of structural optimization, the relatively unstable orientations resulting from our method cannot be obtained.

In this study, a counting method of molecular structures is featured and effects of temperature and pressure on the polymer structures have not been considered. However, the present method is effectively applied to predict molecular structures in molecular dynamics simulations or Monte Carlo methods, in which free energies depending on temperature and pressure are computed.

SPEEK is expected to be a preferable candidate for a proton exchange membrane due to mechanical strength and

thermal stability [25,26,30,32]. However, the proton conductivity is known to be inferior to a major proton exchange membrane Nafion®. In Nafion® membranes, sulfonic groups that contribute to form water channels can flexibly move for their reorientations when water molecules are injected. Water channels are inevitable to enhance the proton conduction. On the other hand, sulfonic groups in SPEEK are directly bonded to main chains and there are no side chains that effectively contribute to the reorientations. In this study, the present method is applied to investigate the possibility of SPEEK forming a preferable structure to make water channels. Consequently, our results indicate that sulfonic groups tend to be distributed homogeneously in SPEEK and that concentrated water channels cannot be expected. Therefore, sufficient humidification is required to form water channels in SPEEK. This suggestion qualitatively confirms the experimental and computational results from SPEEK membranes [27–29,33,34,36,38].

IV. CONCLUDING REMARKS

In the present study, a theoretical procedure to model polymer structures was developed under the assumptions of the symmetry and the periodicity. Based on Burnside's lemma, the number of nonequivalent structures in a symmetric system was counted efficiently, eliminating energetically equivalent structures. A tile painting problem was applied to calculate nonequivalent polymer structures. Computations were performed for one- and two-dimensional alignments and the computational efficiency was improved.

This method was applied to investigate a role of functional groups in polymers. Significant characteristics could be obtained focusing on the distribution of functional groups, although the complexity of the polymer structures was ignored.

Distributions of sulfonic groups in SPEEK were counted completely on the assumption of D_{3h} symmetry. Consequently, it was found that sulfonic groups tend to be dispersed in the polymer structures and that highly oriented structures become unstable relatively. Sulfonic group concentrations that induce water channels to promote proton conduction are predicted to be unfavorable in SPEEK. These results conclude that enough humidification is required to obtain high proton conductivity using SPEEK membranes. On the other hand, the energy stability of the polymer chain bundles indicates the mechanical stability of SPEEK.

[1] F. J. M. Hoeben, P. Jonkheijm, E. W. Meijer, and A. P. H. J. Schenning, Chem. Rev. **105**, 1491 (2005).

[2] K. Doi, K. Yoshida, H. Nakano, A. Tachibana, T. Tanabe, Y. Kojima, and K. Okazaki, J. Appl. Phys. **98**, 113709 (2005).

[3] H. B. Akkerman, P. W. M. Blom, D. M. de Leeuw, and B. de Boer, Nature (London) **441**, 69 (2006).

[4] M. Taniguchi and T. Kawai, Physica E **33**, 1 (2006).

[5] M. Armand and J. M. Tarascon, Nature (London) **451**, 652 (2008).

[6] S. Lu, J. Pan, A. Huang, L. Zhuang, and J. Lu, Proc. Natl. Acad. Sci. USA **105**, 20611 (2008).

[7] K. Doi, K. Kato, and S. Kawano, in *Proceedings of the International Conference on Computational & Experimental Engineering and Sciences, Las Vegas, 2010*, edited by D. W. Pepper and S. N. Atluri (Tech Science Press, Las Vegas, 2010), pp. 330–335.

[8] K. Doi, T. Yonebayashi, and S. Kawano, J. Mol. Struct., Theochem. **939**, 97 (2010).

[9] J. E. Yoo, K. S. Lee, A. Garcia, J. Tarver, E. D. Gomez, K. Baldwin, Y. Sun, H. Meng, T. Q. Nguyen, and Y. L. Loo, Proc. Natl. Acad. Sci. USA **107**, 5712 (2010).

[10] K. Tybrandt, K. C. Larsson, A. Richter-Dahlfors, and M. Berggren, Proc. Natl. Acad. Sci. USA **107**, 9929 (2010).

[11] N. Agmon, Chem. Phys. Lett. **244**, 456 (1995).

[12] D. Marx, M. E. Tuckerman, J. Hutter, and M. Parrinello, Nature (London) **397**, 601 (1999).

[13] U. W. Schmitt and G. A. Voth, J. Chem. Phys. **111**, 9361 (1999).

[14] N. Agmon, Chem. Phys. Lett. **319**, 247 (2000).

[15] M. E. Tuckerman, D. Marx, and M. Parrinello, Nature (London) **417**, 925 (2002).

[16] H. Lapid, N. Agmon, M. K. Petersen, and G. A. Voth, J. Chem. Phys. **122**, 014506 (2005).

[17] J. Han, X. Zhou, and H. Liu, J. Power Sources **161**, 1420 (2006).

[18] J. A. Elliott and S. J. Paddison, Phys. Chem. Chem. Phys. **9**, 2602 (2007).

[19] S. S. Jang, V. Molinero, T. Çağin, and A. G. William III, J. Phys. Chem. B **108**, 3149 (2004).

[20] D. Brandell, J. Karo, A. Liivat, and J. O. Thomas, J. Mol. Model. **13**, 1039 (2007).

[21] K. Malek, M. Eikerling, Q. Wang, Z. Liu, S. Othuka, K. Akizuki, and M. Abe, J. Chem. Phys. **129**, 204702 (2008).

[22] L. Bytautas and D. J. Klein, J. Chem. Inf. Model. **38**, 1063 (1998).

[23] L. Bytautas and D. J. Klein, J. Chem. Inf. Model. **39**, 803 (1999).

[24] A. Misra and D. J. Klein, J. Chem. Inf. Model. **42**, 1171 (2002).

[25] T. Kobayashi, M. Rikukawa, K. Sanui, and N. Ogata, Solid State Ion. **106**, 219 (1998).

[26] S. M. J. Zaidi, S. D. Mikhailenko, G. P. Robertson, M. D. Guiver, and S. Kaliaguine, J. Membr. Sci. **173**, 17 (2000).

[27] K. D. Kreuer, J. Membr. Sci. **185**, 29 (2001).

[28] S. D. Mikhailenko, K. Wang, S. Kaliaguine, P. Xing, G. P. Robertson, and M. D. Guiver, J. Membr. Sci. **233**, 93 (2004).

[29] B. Yang and A. Manthiram, J. Power Sources **153**, 29 (2006).

[30] J. Chen, M. Asano, Y. Maekawa, and M. Yoshida, J. Membr. Sci. **319**, 1 (2008).

[31] J. K. Lee, W. Li, and A. Manthiram, J. Power Sources **180**, 56 (2008).

[32] G. Zhang, T. Fu, K. Shao, X. Li, C. Zhao, H. Na, and H. Zhang, J. Power Sources **189**, 875 (2009).

[33] J. C. Tsai, H. P. Cheng, J. F. Kuo, Y.-H. Huang, and C.-Y. Chen, J. Power Sources **189**, 958 (2009).

[34] S. D. Mikhailenko, F. Celso, and S. Kaliaguine, J. Membr. Sci. **345**, 315 (2009).

[35] E. Spohr, J. Mol. Liq. **136**, 288 (2007).

[36] P. Y. Chen, C. P. Chiu, and C. Hong, J. Power Sources **194**, 746 (2009).

[37] C. V. Mahajan and V. Ganesan, J. Phys. Chem. B **114**, 8357 (2010).

[38] C. V. Mahajan and V. Ganesan, J. Phys. Chem. B **114**, 8367 (2010).

[39] N. G. Bruijn, J. Comb. Theory **2**, 418 (1967).

[40] E. M. Wright, J. Combin. Theory Ser. B **30**, 89 (1981).

[41] K. P. Bogart, Am. Math. Mon. **98**, 927 (1991).

[42] R. A. Brualdi, *Introductory Combinatorics*, 5th ed. (Pearson Prentice Hall, Upper Saddle River, NJ, 2010), pp. 552–558.

[43] Burnside's lemma is also known as the Cauchy-Frobenius theorem. Details about the origin, the historical transition, and its applications to chemical compounds are mentioned in several books: G. Pólya and R. C. Read, *Combinatorial Enumeration of Groups, Graphs, and Chemical Compounds* (Springer-Verlag, New York, 1987), pp. 96–135; A. Kerber, *Applied Finite Group Actions*, 2nd ed. (Springer-Verlag, Berlin Heidelberg, 1999), pp. 53–73.

[44] S. Kawano, Phys. Rev. E **58**, 4468 (1998).

[45] S. Nagahiro, S. Kawano, and H. Kotera, Phys. Rev. E **75**, 011902 (2007).

[46] I. Hanasaki, T. Haga, and S. Kawano, J. Phys. Condens. Matter **20**, 255238 (2008).

[47] I. Hanasaki, H. Takahashi, G. Sazaki, K. Nakajima, and S. Kawano, J. Phys. D: Appl. Phys. **41**, 095301 (2008).

[48] D. A. Case *et al.*, computer code AMBER 10, University of California, San Francisco, 2008.

[49] I. Hanasaki, H. Shintaku, S. Matsunami, and S. Kawano, Comput. Model. Eng. Sci. **46**, 191 (2009).

[50] K. Doi, T. Haga, and S. Kawano, Phil. Trans. R. Soc. A **368**, 2615 (2010).

Research paper

Effects of a perilymphatic fistula on the passive vibration response of the basilar membrane

Takuji Koike [a,*], Chiaki Sakamoto [a], Tasuku Sakashita [a], Ken Hayashi [b], Sho Kanzaki [c], Kaoru Ogawa [c]

[a] Department of Mechanical Engineering and Intelligent Systems, Graduate School of Informatics and Engineering, The University of Electro-Communications, 1-5-1 Chofugaoka, Chofu, Tokyo 182-8585, Japan
[b] Department of Otolaryngology, Shinkawa Clinic, Kanagawa, Japan
[c] Department of Otolaryngology, School of Medicine, Keio University, Tokyo, Japan

ARTICLE INFO

ABSTRACT

In this study, a three-dimensional finite-element model of the passive human cochlea was created. Dynamic behavior of the basilar membrane caused by the vibration of the stapes footplate was analyzed considering a fluid–structure interaction with the cochlear fluid. Next, the effects of a perilymphatic fistula (PLF) on the vibration of the cochlea were examined by making a small hole on the wall of the cochlea model. Even if a PLF existed in the scala vestibuli, a traveling wave was generated on the basilar membrane. When a PLF existed at the basal end of the cochlea, the shape of the traveling wave envelope showed no remarkable change, but the maximum amplitude became smaller at the entire frequency range from 0.5 to 5 kHz and decreased with decreasing frequency. In contrast, when a PLF existed at the second turn of the cochlea, the traveling wave envelope showed a notch at the position of the PLF and the maximum amplitude also became smaller. This model assists in elucidating the mechanisms of hearing loss due to a PLF from the view of dynamics.

© 2011 Elsevier B.V. All rights reserved.

1. Introduction

The mammalian cochlea consists of a fluid-filled duct that is coiled like a snail shell. The cochlea is divided into three compartments, i.e., the scala vestibuli, the scala media, and the scala tympani, by two longitudinal membranes, i.e., Reissner's membrane and the basilar membrane (BM). The vibration of the tympanic membrane (TM), which is induced by sound, is transmitted to the cochlear fluid through the ossicular chain. The vibration of the cochlear fluid generates a traveling wave on the BM. Auditory sensory cells, which are lined up on the BM, also vibrate in response to the vibration of the BM. The sensory cells transform the vibration of the BM into action potentials in auditory nerve fibers. Therefore, the vibration of the BM is closely related to auditory activity. Ren (2002) achieved vibration measurement of the BM under normal physiological conditions. However, observation of the entire vibration of the BM under physiological conditions is difficult because the bony wall of the cochlea surrounds the BM. To estimate the vibration of the BM under physiological conditions in detail, some theoretical studies have investigated the vibration of the BM using the Wentzel–Kramers–Brillouin (WKB) method (Steele and Taber, 1979; Lim and Steele, 2002; Yoon et al., 2007) or the finite-element method (Böhnke and Arnold, 1999; Manoussaki and Chadwick, 2000; Parthasarathi et al., 2000; Andoh et al., 2005; Skrodzka, 2005; Ramamoorthy et al., 2007; Meaud and Grosh, 2010; Fleischer et al., 2010).

A perilymphatic fistula (PLF) entails pathological connections between the perilymphatic space of the labyrinth and the middle ear (outer fistula) or the cerebrospinal fluid (inner fistula). These abnormal connections clinically have been considered to lead to hearing loss. Indeed, the round window (RW) and oval window (OW) fistula are frequently observed diseases resulting in hearing loss (Goto et al., 2001). However, Weisskopf et al. (1978) noted that hearing loss experimentally was not caused by the leakage of perilymphatic fluid alone. Therefore, the potential causes of this hearing loss associated with PLF have been postulated to include: a double-membrane break (Simmons, 1979), a floating labyrinth (Nomura and Hara, 1986; Nomura et al., 1992), a perilymphatic hemorrhage (Merchant et al., 2005), a pneumolabyrinth (Nishioka and Yanagihara, 1986; Foster and Luebke, 2002), a bony third window (Merchant and Rosowski, 2008) as well as from other

---

Abbreviations: BM, basilar membrane; CF, characteristic frequency; FE, finite element; IHC, inner hair cells; OHC, outer hair cells; OW, oval window; PLF, perilymphatic fistula; RW, round window; ST, scala tympani; SV, scala vestibuli; TM, tympanic membrane.
* Corresponding author. Tel./fax: +81 42 443 5818.
E-mail address: koike@mce.uec.ac.jp (T. Koike).

causes. However, the mechanisms that lead to hearing loss in these matters are unclear.

In this study, the dynamic behavior of the BM and the cochlear fluid caused by the vibration of the stapes were analyzed using a three-dimensional finite-element model of the human cochlea, and the effects of a fistula on the vibration of the BM were analyzed.

2. Model

2.1. Geometry

Fig. 1 shows a Finite-Element (FE) model of the human cochlea. Although the cochlear takes a spiral form, the shape of the FE model was straightened out. As a preliminary investigation, a spiral-shaped model was made, and the results were compared to those obtained from the straight model. The points of maximum amplitude on the BM in the spiral-shaped model were shifted to the basal region by 6% (at high frequencies) to 10% (at low frequencies) compared with those in the straight model. The peak amplitude in the spiral-shaped model was reduced by up to 6% at low frequencies. Although slight changes were observed, the difference in the vibration behavior of the BM between the two models was not in general remarkable. Therefore, to avoid complications of the analysis, the straight model is used in this paper.

The straight model consists of structural parts and liquid parts. The structural parts are the stapes, the stapedial annular ligament, the OW membrane, the RW membrane, the BM, and the osseous spiral lamina. The liquid parts are the vestibule, the scala vestibuli, the scala tympani, and the cochlear aqueduct, which are all filled with lymphatic fluid. To avoid complication of the analysis, the structures in the cochlea were simplified as follows. Although the inner hair cells (IHC), the outer hair cells (OHC), and supporting cells exist on the BM, these cells were ignored, and the BM was assumed to be a thin flat membrane. Accordingly, the active cochlear mechanism of amplification related to the electromotility of the OHCs was not included. Reissner's membrane was also ignored in this model, and the lymphatic fluid area was divided into two compartments by the BM and the osseous spiral lamina. These two liquid compartments, i.e., the scala vestibuli and the scala tympani, were connected at the helicotrema. The scala vestibuli and the scala tympani were considered as rectangular ducts, and the outer shape of the cochlea was assumed to change linearly from base to apex.

The volume of the lymphatic fluid, the width and thickness of the BM, the area and thickness of the RW membrane were determined based on data previously reported (Ulehlova et al., 1987; Igarashi et al., 1986; Becvarovski, 2004; Wever, 1949; Koike et al.,

2002). Specifically, regarding the shape of the BM, its width was assumed to be 100 μm at the basal part and 500 μm at the apex, and to change linearly from base to apex. In the same way, its thickness was assumed to be 30 μm at the basal part and 10 μm at the apex. The dimensions of the cochlear model are summarized in Fig. 2 and Table 1.

2.2. Mechanical properties and boundary conditions

The mechanical properties of each part of the model were determined based on previous reports (Andoh and Wada, 2004; Koike et al., 2002; Lim et al., 2005). The reported value of the Young's modulus of the BM was slightly modified so that our numerical results correspond with the measurements results. Young's modulus for the RW membrane was assumed to be the same as that of the TM (Koike et al., 2002). In the previous study (Koike et al., 2002), a simple stapes model consisting of only the stapes, stapedial annular ligament, and loading of the cochlea damping was established, and Young's modulus for the stapedial annular ligament was determined so that the impedance of the stapes corresponds with the measurement result of the stapes impedance (Merchant et al., 1996). In this study, the OW membrane was newly considered, and the values of the unknown mechanical properties of the OW membrane were determined to optimize the impedance of the stapes. However, the contribution of the stiffness of the OW membrane is much smaller than that of the annular ligament because the OW membrane is thinner than the annular ligament. In addition, because the thickness of the OW membrane is unclear, the mechanical properties of the OW membrane may have margins of error.

Rayleigh damping parameters affect the shape of the traveling wave. The parameters were determined so that the envelope of the traveling wave was similar to the measurement results (Ren, 2002). The BM consists of collagen fibers embedded in a ground substance and appears to be an anisotropic material (Iurato, 1962; Cabezudo, 1978; Schweitzer et al., 1996; Dreiling et al., 2002). Fleischer et al. (2010) reported that spatial variation in the compliance of the BM in both the longitudinal and radial directions is partially caused by the anisotropy. However, the BM is considered to be an isotropic material in this model. The mechanical properties used for the model are summarized in Table 2.

The extremities of the BM, the RW membrane, and the stapedial annular ligament were rigidly fixed. Because the real cochlea is embedded in the temporal bone, the walls of the vestibule, the scala vestibuli and the scala tympani were assumed to be rigid walls. At the end of the cochlear aqueduct on the subarachnoid space side, the pressure fluctuation caused by the stapes vibration was assumed to be negligible, and the boundary condition for the
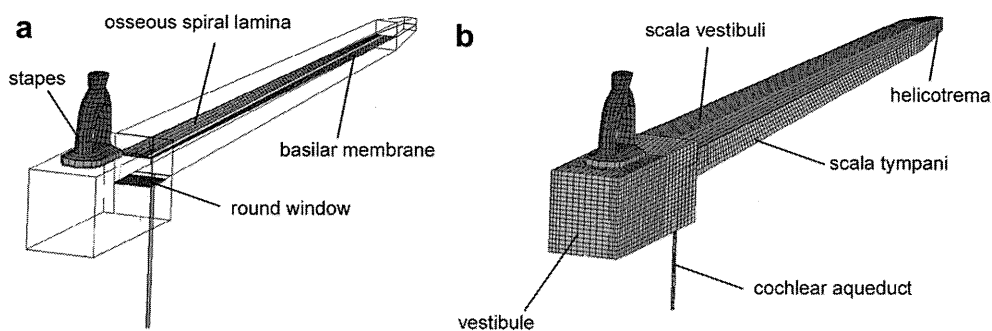

Fig. 1. Finite-element model of the human cochlea. (a) Structural parts. (b) Liquid parts. The OW membrane covers the OW and sticks to the flat surface of the stapes footplate. The OW membrane, the RW membrane, and the BM were meshed by four-noded shell elements. Other parts were meshed by eight-noded hexahedral elements. The total numbers of the nodes and elements were 41,912 and 28,393, respectively.
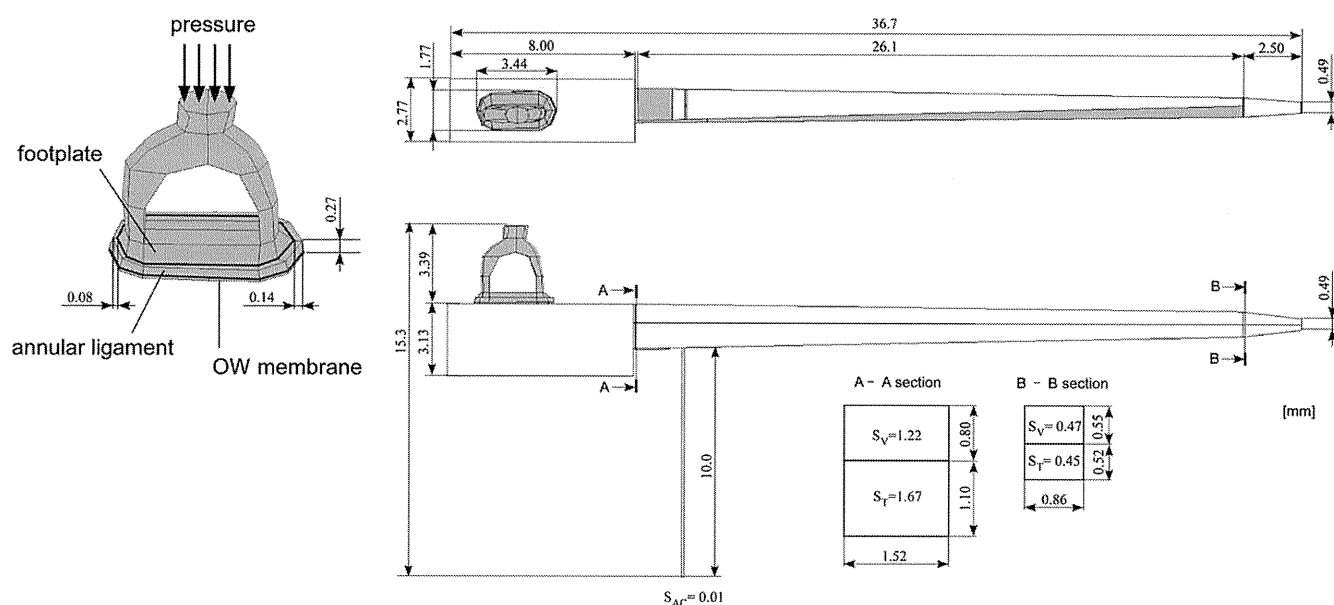
Fig. 2. Dimensions of the cochlear and stapes model. S_V, S_T, and S_{AC} are a cross-section area of the SV, the ST, and the cochlear aqueduct (unit is mm²). Stapedial annular ligament binds the edge of the stapes footplate to the rim of the OW. The OW membrane covers the inner surfaces of the stapes footplate and the stapedial annular ligament. The stapedial annular ligament and the OW membrane were fixed at the rim of the OW. The arrows show the area where the pressure was applied.

end of the cochlear aqueduct (at the lower end of the aqueduct in Fig. 1) was set to be "outlet", and the pressure fluctuation of the lymphatic fluid at the face of the outlet was fixed at zero. That is, the lymphatic fluid was assumed to be able to flow without restraint at the outlet.

To investigate the effects of a fistula on the vibration of the BM, a small outlet was opened on the bony wall of the cochlea as shown in Fig. 3. Although the size of a real fistula is usually not measured during surgery, it is estimated to be small (Ikezono et al., 2010). In this study, micro-sized outlets were made. The shapes of the outlets were assumed to be rectangle, and the areas and aspect ratios of each outlet are shown in Table 3.

For each frequency, a single sinusoidal tone of pressure amplitude of 0.2 Pa was applied to the surface of the stapes head (Fig. 2), and the induced vibration of the lymphatic fluid and structures

Table 1
Dimensions of the cochlear model.

Cochlea	
Length[a]	28.6 mm
Basilar membrane[d]	
Length	26.1 mm
Width	
Base	100 μm
Apex	500 μm
Thickness	
Base	30 μm
Apex	10 μm
Cochlear fluid (volume)[b]	
Total fluid space	118.2 mm³
Cochlear space	48.8 mm³
Vestibular space	69.4 mm³
Round window membrane[c]	
Area	2.21 mm²
Thickness	60 μm
Oval window membrane	
Area[e]	4.22 mm²
Thickness	60 μm

[a] Ulehlova et al. (1987).
[b] Igarashi et al. (1986).
[c] Becvarovski (2004).
[d] Wever (1949).
[e] Koike et al. (2002).

Table 2
Mechanical properties used in the model.

Cochlear fluid	
Density[a]	1.034×10^3 [kg/m³]
Viscosity	2.8×10^{-3} [N s/m²]
Basilar membrane[a]	
Young's modulus	6.33×10^6 [Pa]
Poisson's ratio	0.49
Density	1.2×10^3 [kg/m³]
Round window membrane	
Young's modulus	3.34×10^7 [Pa]
Poisson's ratio	0.49
Density	1.2×10^3 [kg/m³]
Oval window membrane	
Young's modulus	3.34×10^6 [Pa]
Poisson's ratio	0.49
Density	1.2×10^3 [kg/m³]
Osseous spiral lamina[c]	
Young's modulus	2.0×10^{11} [Pa]
Poisson's ratio	0.3
Density	1.2×10^3 [kg/m³]
Stapes[b]	
Young's modulus	1.2×10^{10} [Pa]
Poisson's ratio	0.3
Density	2.75×10^3 [kg/m³]
Stapedial annular ligament[b]	
Young's modulus	4.9×10^5 [Pa]
Poisson's ratio	0.3
Density	2.5×10^3 [kg/m³]
Rayleigh damping parameters	
α	10020 [1/s]
β	6.43×10^{-7} [s]

[a] Andoh and Wada (2004).
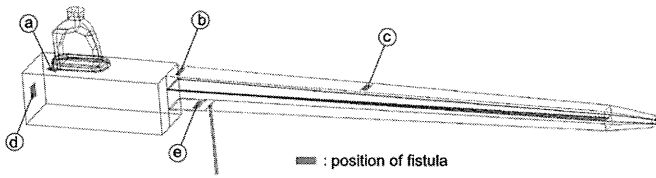[b] Koike et al. (2002).
[c] Lim et al. (2005).

Fig. 3. Position of the fistula on the bony wall of the cochlea. The fistula was opened adjacent to the OW (a), at the basal part of the SV (b), center part of the SV (c), vestibule (d), and adjacent to the RW (e). The fistulas are not drawn to scale.

were calculated. Because the effective area ratio of the stapes head to the TM in this model and the low-frequency lever ratio for the ossicles are 7.8×10^{-3} and 1.3, respectively, the middle ear pressure gain is 44 dB. Therefore, the 0.2 Pa at the stapes head is equivalent to 36 dB at the TM at low frequencies.

2.3. Formulation

All calculations in this study were done using CFD-ACE+ software (ESI CFD Inc.). CFD-ACE+ is a Computational Fluid Dynamics and Multiphysics software. It enables coupled simulations of fluid, thermal, chemical, biological, electrical and mechanical phenomena. In this study, the fluid–structure interaction was considered. Macroscopic fluid response is assumed to be incompressible, and thus an incompressible Navier–Stokes equation is used to analyze the dynamic behavior of the lymphatic fluid. The incompressible Navier–Stokes equation is as follows:

$$\frac{\partial \mathbf{v_f}}{\partial t} + \left(\mathbf{v_f} \cdot \nabla\right)\mathbf{v_f} + \frac{1}{\rho}\nabla p - v\Delta\mathbf{v_f} = 0, \tag{1}$$

where $\mathbf{v_f}$ is the fluid velocity vector, ρ is the fluid density, p is the fluid pressure caused by the motion of the structure, v is the kinematic viscosity of the fluid, t is the time, and the gradient operator ∇ and the Laplacian operator Δ are defined in the following form

$$\nabla = \left(\frac{\partial}{\partial x}, \frac{\partial}{\partial y}, \frac{\partial}{\partial z}\right), \Delta = \frac{\partial^2}{\partial x^2} + \frac{\partial^2}{\partial y^2} + \frac{\partial^2}{\partial z^2}. \tag{2}$$

In the structure model, the equation of the motion is represented by the following matrix differential equation:

$$[M]\frac{\partial^2 \mathbf{u_s}}{\partial t^2} + [C]\frac{\partial \mathbf{u_s}}{\partial t} + [K]\mathbf{u_s} = \mathbf{f}, \tag{3}$$

where $[M]$, $[C]$, and $[K]$ are the mass, damping, and stiffness matrices, respectively, $\mathbf{u_s}$ is the structural displacement vector, $\mathbf{f}$ is the force vector, and t is the time. The damping matrix $[C]$ is derived from the linear combination of mass and stiffness matrices, i.e.,

$$[C] = \alpha[M] + \beta[K], \tag{4}$$

where α and β are Rayleigh damping parameters. The values of the vectors at each time step were obtained using the Newmark-β algorithm.

This analysis used the two-way coupling option. A converged steady-state flow field was obtained, and then the pressure loading

Table 3
Area of the fistula.

Position	Area (mm²)	Aspect ratio
a	0.117	1.50
b	0.075	1.19
c	0.062	1.12
d	0.082	1.32
e	0.764	2.82

from that flow field was applied to the Stress Module to calculate the resulting stresses. Next, the geometry deformations from the structural analysis were fed back to the Flow Modules. The Navier–Stokes Eq. (1) contains a nonlinear term, and the nonlinear fluid motion is coupled back into the right hand side of the kinematic Eq. (3) for the structure model. Consequently, the BM also shows nonlinear motion. However, in a preliminary investigation, the nonlinear component of the BM vibration was too small, and the amplitude of the BM vibration linearly increased by increasing the applied pressure to the stapes head in the pressure range from 0.2 Pa (36 dB at the TM) to 20 Pa (76 dB). The nonlinearity originated in the response of the lymphatic fluid is therefore negligible in this study.

The OW membrane, the RW membrane, and the BM were meshed by Solid Shell Elements. Other parts were meshed by Standard Elements (eight-noded hexahedral elements). The BM was divided equally into 99 elements longitudinally and four elements transversally. The total numbers of the nodes and elements were 41,912 and 28,393, respectively.

3. Results

3.1. Traveling wave and tonotopic map

Fig. 4 shows the time course of the vibration of the BM at 0.5 and 5 kHz obtained using the FE model. A traversing wave was generated on the BM by vibrating the stapes head, and the position where the traveling wave reached its maximum amplitude was changed according to the stimulus frequency. Greenwood reported the relationship between the frequency of the sound applied to the cochlea and the position where the vibration of the BM shows the maximum amplitude based on measurement results; in other words, the distribution of the characteristic frequency (CF) of the BM (Greenwood, 1990). The dashed line in Fig. 5 shows this relationship. The vertical axis shows the frequency of the sound applied to the cochlea, and the horizontal axis shows the normalized position of the BM from base to apex. The dots in Fig. 5 show the numerically obtained results. Although points of the numerical results lie consistently above the dashed line (about 0.6 oct), the CF distribution obtained from the model is reasonable.

Fig. 6 shows the ratio of the amplitude of the BM to the amplitude of the stapes footplate at the position where the CF of the BM is 2.0 kHz. The numerically obtained results shown by the dots have a similar tendency to the measurement result (Stenfelt et al., 2003) shown by the dashed line although the measurement result has some peaks and notches.

3.2. Effect of the fistula on the vibration of the basilar membrane

Fig. 7 shows the time course of the vibration of the BM at 1.0 kHz. The shape of the traveling wave envelope showed no remarkable change when the fistula existed adjacent to the OW (a in Fig. 3), at the basal end of the cochlea (b), and at the vestibule (d). However, the maximum amplitudes of the BM in these cases were smaller than that in the intact cochlea (f) by 11.4 dB, 8 dB and 5.5 dB, respectively. By contrast, when the fistula existed at the center part of the scala vestibuli (c) (12.8 mm from the basal end, CF is 2 kHz), both the shape and amplitude of the traveling wave changed. The envelope of the traveling wave has a notch at the position where a fistula exists, and the maximum amplitude was reduced by 8.4 dB. Fig. 8 shows the time course of the vibration of the BM for stimulus frequencies of 0.5, 1.0 and 2.0 kHz when a fistula exists at the center part of the scala vestibuli. The notch at the position where the fistula exists was remarkable when the input frequency was lower than the CF at the position where the fistula existed. The notch became unclear with increasing input
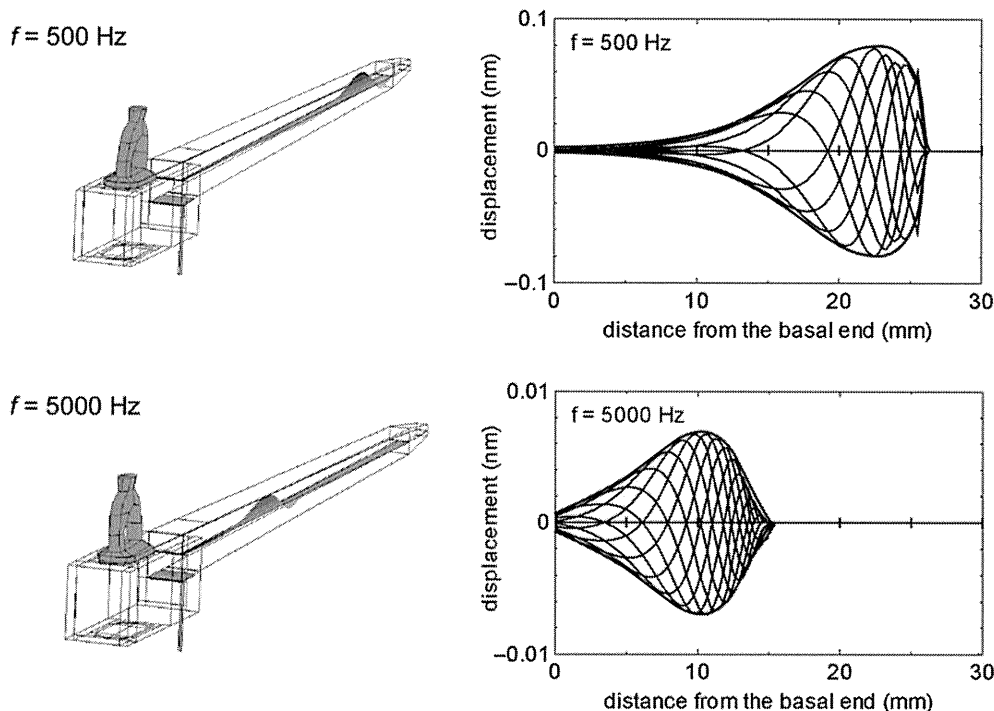
$f = 500$ Hz

$f = 5000$ Hz

Fig. 4. Time course of BM vibrations in normal cochlea. A small shift (10% of the maximum amplitude) is generated at the basal end ($x = 0$) when $f = 5.0$ kHz.

frequency, and disappeared when the input frequency came close to or exceeded the CF at the position where the fistula existed.

Fig. 9 shows the time course of the vibration mode of the BM and the pressure difference between the scala vestibuli and scala tympani at the surfaces of the BM. In the intact cochlea, the pressure difference was relatively large at the basal part of the cochlea and decreased gradually from base to apex. By contrast, in the case of the cochlea with a fistula at the center part of the scala vestibuli, the pressure difference rapidly decreased to the part where the fistula existed.

The ratio of the maximum amplitude of the BM with a fistula to that in the intact cochlea is shown in Fig. 10. When the fistula was opened at the vestibule (a, d) or at the scala vestibuli (b, c), the maximum amplitude of the BM was smaller than that in the intact cochlea, and the BM amplitude decreased with decreasing frequency. By contrast, when the fistula existed at the vicinity of the RW (e), the shape of the traveling wave envelope and the maximum amplitude were scarcely changed. Regarding the place of maximum BM amplitude, no significant change was observed between before
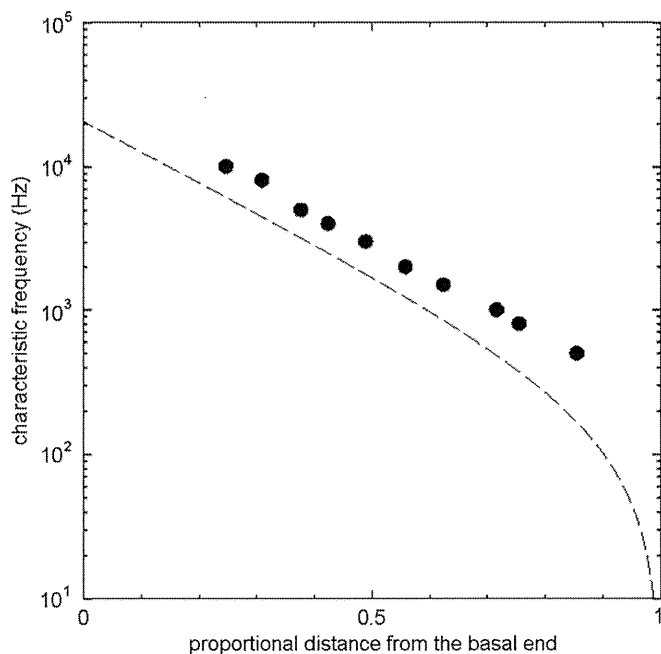

Fig. 5. Distribution of the characteristic frequency of the BM. The dashed line shows the measurement results by Greenwood (1990), and dots show the numerical results.
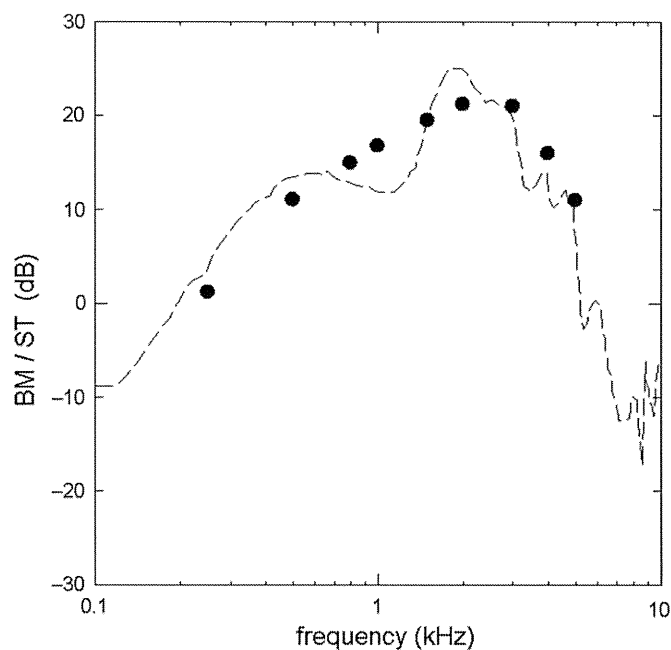
Fig. 6. BM velocity relative to stapes footplate velocity. The dashed line shows the measurement results by Stenfelt et al. (2003), and the dots show the numerical results.
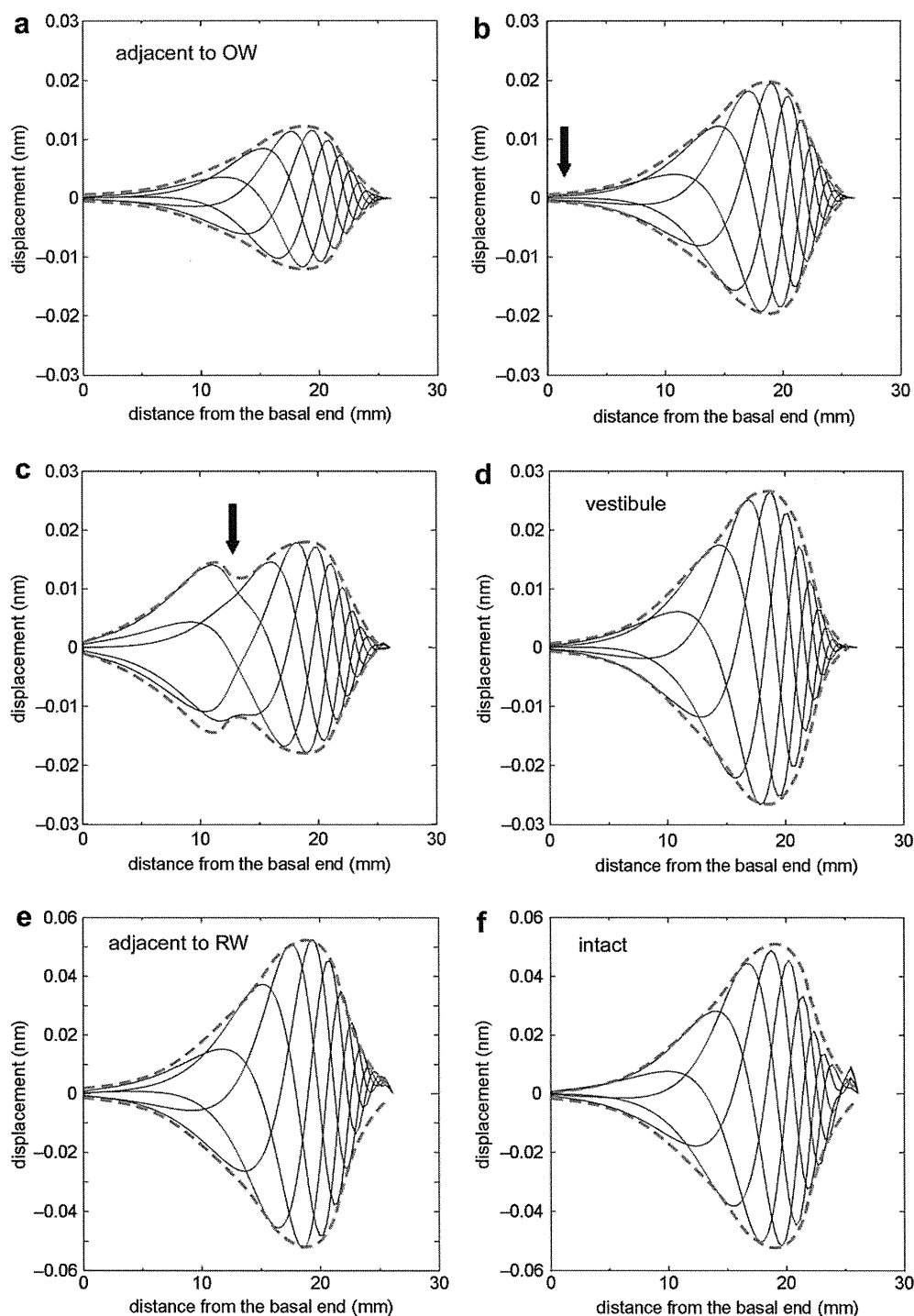
95

Fig. 7. Time course of BM vibrations when a fistula exists. Applied frequency is 1.0 kHz. (a) the fistula exists adjacent to the OW, (b) at the basal part of the SV, (c) center part of the SV, (d) vestibule and (e) adjacent to the RW. (f) Intact cochela. Phase interval is $2\pi/5$. Arrows show the position of the fistula.

and after opening the fistula at the frequencies at which the results were obtained.

4. Discussion

4.1. Relevance of the model

When a fluid pressure fluctuation is induced by vibration of the stapes, two types of pressure waves occur in the cochlea (Lighthill, 1981). One is a fast wave which is a compressional wave caused by the stapes vibration. It is uniformly distributed over the cross-section of each scala, and propagates at the velocity of sound. The magnitude difference of the fast wave between the SV and the ST is possibly caused by the stiffness and damping of the BM. The other is a slow wave which results from a fluid flow according to the interaction between the BM and the lymphatic fluid, and the slow wave follows a traveling wave on the BM. The slow wave exists in the vicinity of the BM and has equal magnitude with opposite phases at either side of the BM. The fast wave travels at 1400 m/s, and the speed of energy flow of the slow wave falls from around
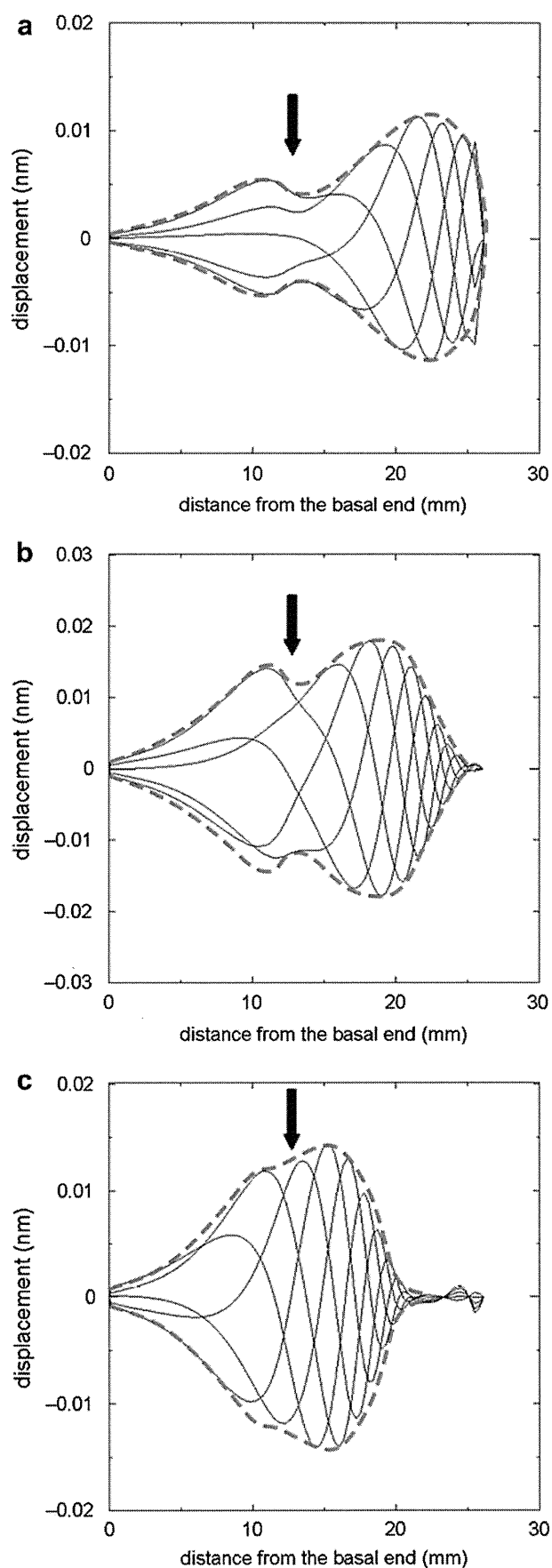
100 m/s at the base to zero at the position of resonance (Lighthill, 1981). The wavelengths of the fast wave and the slow wave are estimated to be 280 mm and 20–0 mm for a stimulation of 5 kHz, respectively. The wavelengths of the fast wave are much longer than the length of the cochlea model (36.7 mm); therefore, the assumption of the incompressible fluid is acceptable. In contrast, the wavelength of the slow wave can be shorter than the size of the liquid elements (0.26 mm) near the position of resonance. There-fore, the slow wave at the neighborhood of the portion of resonance may not be accurately estimated. However, the wavelength of the slow wave is approximately 3 mm at the apical side of the position of the resonance, and the amplitude of the slow wave becomes smaller toward the apical part as shown in Fig. 9 ($f = 1.0$ kHz). This wavelength is relatively longer than the size of the liquid elements, and the contribution of the pressure of the slow wave at the apical side away from the resonance position is negligible. The same can be said for other frequencies. Therefore, the contribution of the locally generated slow wave near the BM at the resonance position is believed to be reasonably considered in this model.

The CF distribution is determined by the distribution of the thickness and mechanical properties of the BM. However, deter-mining the proper values in the human cochlea is difficult at present. Therefore, we assumed simple shape and mechanical properties, and checked the validity of the model as a whole by comparing the numerically obtained CF distribution with that obtained by Green-wood (Fig. 5). Our results were plotted consistently above Green-wood's map. Greenwood's map is for active conditions whereas our model is passive. This may be one reason for the model CF values lying consistently above Greenwood's CF map. However, the CF distribution is susceptible to the effect of the stiffness of the BM. When Young's modulus of the BM was reduced to 40% of the value presented in Table 2, the numerical results were in good agreement with the Greenwood's map. In addition, as described in the Geom-etry section, the spiral shape of the cochlea also affects the CF distribution. The spiral shape contributes to shifting the CF of a certain position of the BM to low frequency. Therefore, Young's value of the BM in Table 2 was used for the straight model. Although there is still room for improvement, the model herein presented is believed to have reasonable validity and to be able to simulate the dynamic behavior of the cochlea at medium to high SPLs.

4.2. Shape of the envelope of the traveling wave

The mechanism of hearing loss directly caused by existence of PLF has not been clarified so far. Hence, the potential causes of hearing loss associated with PLF such as double-membrane break theory (Simmons, 1979), floating labyrinth (Nomura and Hara, 1986; Nomura et al., 1992), perilymphatic hemorrhage (Merchant et al., 2005), pneumolabyrinth (Nishioka and Yanagihara, 1986; Foster and Luebke, 2002), and a bony third window (Merchant and Rosowski, 2008) have been postulated. However, the effects of mixing of the endolymph and perilymph were not examined here because Reissner's membrane has been neglected and the lymph in the cochlea is assumed to be homogeneous in the current cochlear model presented in this study. These effects should be included in the future. However, at this stage, the effects of the existence of PLF by itself on the vibration of the BM were examined here from the view of dynamics.

Fig. 8. Time course of BM vibrations when a fistula exists at the center part of the SV. (a) 0.5 kHz, (b) 1.0 kHz, (c) 2.0 kHz. Phase interval is $2\pi/5$. Arrows show the position of the fistula. The small displacement of the BM found at the apical region is the transient response generated shortly after applying the sinusoidal vibration to the stapes. This small displacement disappeared within a few cycles.
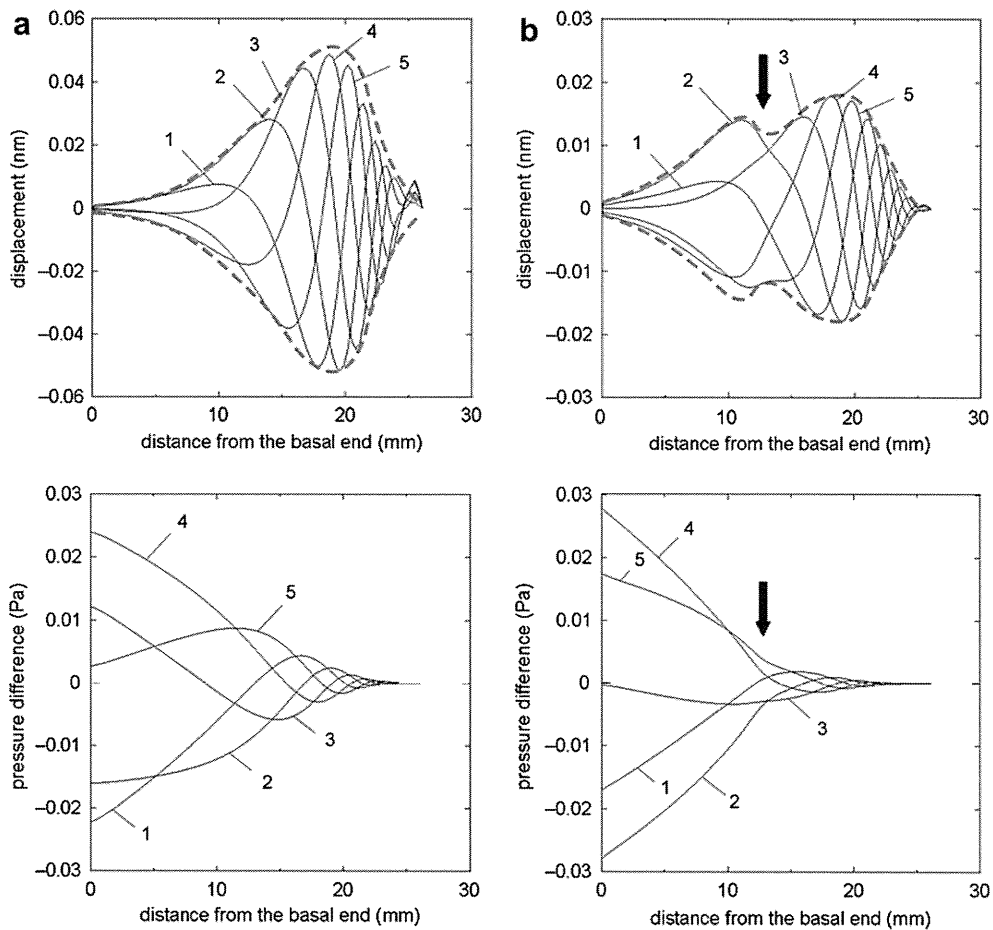
Fig. 9. Time course of BM vibrations and pressure difference between SV and ST. Frequency is 1.0 kHz. Phase interval is $2\pi/5$. The numbers present the time course. (a) Intact cochlea. (b) Cochlea with a fistula at the center part of the scala vestibuli. Arrow shows the position of the fistula.
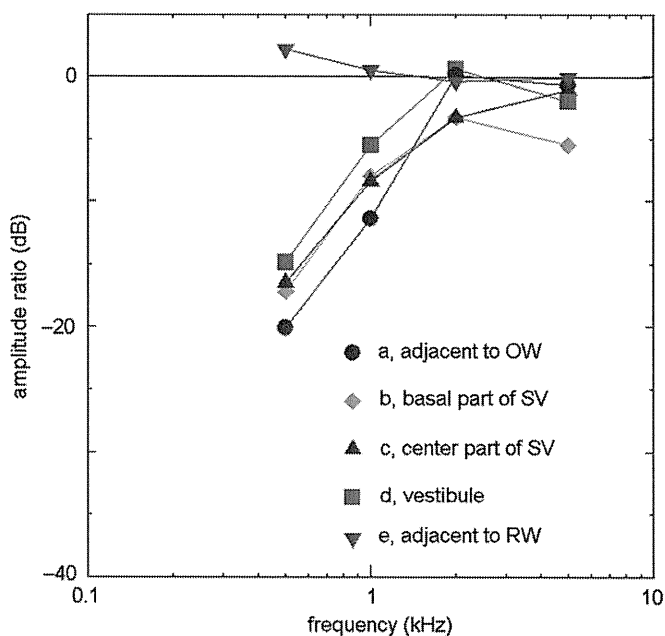

Fig. 10. Ratio of the maximum amplitude of the BM in the cochlea with a fistula to that in the intact cochlea.

The effects of the fistula on the vibration of the BM were different according to the position of the fistula and to the applied frequency as shown in Figs. 7–9. As shown in Fig. 9, when a fistula exists at the center part of the scala vestibuli and the applied frequency is lower than the CF of the part where the fistula exists, the amplitude of the BM decreases at the part where the fistula existed, resulting in two peaks in the BM amplitude response (wave envelope). The BM is excited by the pressure difference between the scala vestibuli and scala tympani. When a fistula exists on the wall of the scala vestibuli, the pressure of the scala vestibuli falls down in the area from the part of the fistula to apex, and the exciting force acting on the BM is also consequentially reduced. The amplitude at that area is therefore reduced. However, the original peak of the BM still exists in that area. These are reasons why the BM has two peaks and a notch when a fistula exists on the wall of the scala vestibuli and frequencies lower than the CF are applied to the cochlea. This result suggests that the BM in the real cochlea possibly has two peaks in its motion according to the position of a fistula, and the change in the shape of the traveling wave envelope may affect speech recognition.

4.3. Vibration amplitude of the basilar membrane

The maximum amplitude of the BM was reduced at low frequencies below 2 kHz when a fistula existed at the vestibule or at the scala vestibuli (Fig. 10). The vibration of the BM became small especially at low frequencies when the fistula existed at the